Article

Estimation of Land Surface Temperature from CHINESE ZY1-02E IRS Data

Xianhui Dou , Kun Li , Qi Zhang , Chenyang Ma , Hongzhao Tang , Yonggang Qian * , Jun Chen , Jinglun Li , Yichao Li , Tao Wang , Feng Wang , Juntao Yang , Xining Liu

Posted Date: 6 December 2023

doi: 10.20944/preprints202312.0301.v1

Keywords: land surface temperature; WVS-based LST method; ZY1-02E IRS

Article

Estimation of Land Surface Temperature from CHINESE ZY1-02E IRS Data

Xianhui Dou [1,2], Kun Li [3], Qi Zhang [3,4,6], Chenyang Ma [3,6], Hongzhao Tang [2], Yonggang Qian [3,4]*, Jun Chen [1], Jinglun Li [3,4,6], Yichao Li [3,4,6], Tao Wang [3,4,6], Feng Wang [7], Juntao Yang [7] and Xining Liu [5,]*

[1] Xi'an Jiaotong University, Shanxi 710049, China
[2] Land Satellite Remote Sensing Application Center, Ministry of Natural Resources, Beijing 100094, China
[3] Key Laboratory of Digital Earth Sciences, Aerospace Information Research Institute, Chinese Academy of Sciences, Beijing 100094, China
[4] International Research Center of Big Data for Sustainable Development Goals, Beijing 100094, China
[5] China Sanya Institute of South China Sea Geology, Guangzhou Marine Geological Survey, Sanya 572025, China
[6] University of Chinese Academy of Sciences, Beijing 100049, China
[7] The Fourth Topographic Survey Team, Ministry of Natural Resources, Harbin 150028, China
* Correspondence: qianyg@aircas.ac.cn Tel.: +86-10-82177498; liuxining@mail.CGS.gov.cn Tel.: +86-13891842073

Abstract: The role of land surface temperature (LST) is of utmost importance in multiple academic disciplines such as climatology, hydrology, ecology, and meteorology. Until to now, many methods have been proposed to estimate LST from satellite thermal infrared data. The Thermal Infrared Sensor (IRS) on the Chinese ZY1-02E satellite is a pivotal instrument employed for gathering thermal infrared (TIR) data of land surfaces. The objective of this research is to evaluate the feasibility of a single-channel approach based on water vapor scaling (WVS) for deriving LST from ZY1-02E IRS data because of its wide spectrum range, i.e., 7~12μm, affected strongly by both atmospheric water vapor and ozone. Three study areas, namely Baotou, Heihe River Basin, and Yantai-sea sites, were selected as validation sites to evaluate the LST inversion accuracy. This evaluation was also conducted by cross-comparison between the retrieved LST and MODIS LST product. The results revealed that the WVS-based method exhibited an average bias of 0.63K and an RMSE of 1.62K compared to the in-situ LSTs. The WVS-based method demonstrated reasonable accuracy through cross-validation with the MODIS LST product, with an average bias of 0.77K and RMSE of 2.0K. These findings provide that the WVS-based method is effective to estimate LST from ZY1-02E IRS data.

Keywords: land surface temperature; WVS-based LST method; ZY1-02E IRS

1. Introduction

Land surface temperature (LST) is a crucial parameter in multiple fields of study, such as climatology[1-5], ecology[6, 7], and surface energy [8-10]. It is widely recognized as a significant Earth surface parameter[11] and is considered one of the ten essential climate variables in the land biosphere, as defined by the Global Climate Observing System [12, 13].

Satellite observations offer a precise method for obtaining LST on a global scale, thanks to their large spatial resolution and regular temporal revisiting[14]. In the past decades, various algorithms have been developed to retrieve LST from thermal infrared instruments carried on satellites, such as the single-channel (SC) algorithm[15-17], the split-window (SW) algorithm[18, 19], multiple angle methods[18, 20-22], and the temperature and emissivity separation (TES) algorithm[23-27], etc. A comprehensive overview of LST retrieval methods can be seen in previous research[13, 14]. Except for the single-channel methods, all the other methods require two or more thermal infrared channels. Single-channel method has been applied to the Landsat platform, which has one thermal channel. Traditionally, the main disadvantage of this method is that it requires atmospheric parameters and land surface emissivity as prior knowledge.

ZY1-02E satellite was successfully launched on December 26, 2021, from the Taiyuan Satellite Launch Centre, China, aboard a Long March-4 carrier rocket. Developed by the Fifth Academy of Aerospace Science and Technology Corporation, the ZY1-02E satellite is classified as a medium-resolution remote sensing satellite. Its primary purpose is to conduct land resources survey and monitoring, providing domestic data support for the investigation, monitoring, supervision and production capacity monitoring of land resources. Additionally, it contributes to disaster reduction, environmental protection, housing and construction, transportation, agriculture, forestry, marine surveying and mapping industries.

The ZY1-02E satellite carries a payload comprising three instruments—the Visible Near-Infrared Multispectral Camera (VNIC), the Advanced Hyperspectral Imager (AHSI) and the Thermal Infrared Sensor (IRS). The AHSI instrument features 166 bands, offering a resolution of 30 m and a width of 60 km. The VNIC sensors provide a panchromatic imagery at 2.5 m resolution and multispectral data with 8 bands at 10 m resolution covering a width of over 100 km. The IRS has a single thermal infrared band, providing a spatial resolution of 16 m and covering a width of 60 km.

Unlike traditional thermal sensor, ZY1-02E IRS sensor has a wider spectral coverage, i.e., 7~12μm, which includes a stronger atmospheric water vapor absorption and ozone absorption bands. This study aims to evaluate the feasibility of temperature inversion using a single channel algorithm based on WVS from ZY1-02E single-channel IRS data because of its wide spectrum range affected by both atmospheric water vapor and ozone. The organization structure of paper is as follows: Section 2 introduces the used ZY1-02E IRS and VNIC data, atmospheric profiles, and in-situ field measurements. Sections 3 shows the WVS-based LST inversion method. Section 4 and Section 5 gives the results and discussion. Section 6 is the conclusions.

2. Study Area and Data

2.1. Study Area

Field campaigns were conducted to validate the accuracy of the algorithms using ZY1-02E IRS data. For validation purposes, three field sites were chosen: Baotou, Heihe, and Yantai-Sea. The selection of these three sites mainly considers regional differences, climate differences and surface type differences, which can have a more comprehensive evaluation of temperature inversion.

The Baotou site is located in Urad Front Banner, in western Inner Mongolia, with coordinates of approximately 40.85°N latitude and 109.6°E longitude. The Baotou site encompasses two different target categories for validation. The first category consists of a crop target measuring 300m×600m, primarily comprising corn, which is ideal for validating LST. The second category comprises a desert target, measuring around 300m×300m. Figure 1 shows both the crop target and natural desert target at the Baotou site, with a separation distance of approximately 6 km between them. Water bodies serve as natural targets for thermal infrared calibration and validation due to their high thermal inertia and minimal spatiotemporal temperature variability. Thus, Ulansuhai Lake, located in the Urad Qianqi, was used to obtain the water temperature for validation. Additionally, bare soil and Kubq desert surrounding Ulansuhai Lake were also selected for validation purposes. The Baotou site and Ulansuhai Lake have average ground elevations of 1290 m and 1021 m, respectively.

The Heihe River Basin (HRB) serves as the second site in this study. Situated in the arid region of northwestern China, it is the second largest endorheic basin in China. The HRB is well-suited for investigating land surface processes due to its diverse landscapes[28]. The hydrometeorological observatory consists of over 20 observation stations that cover the main land surfaces in the HRB. These surfaces include alpine meadows, forestlands, croplands, deserts, bare lands, and wetlands. For the purposes of validation, two stations, namely Zhangye wetland and Desert, are chosen. These stations are located in the upstream region, midstream region and downstream region in the HRB, respectively.

The third site, Yantai-sea, is located in the eastern China at a latitude of 37.51°N and a longitude of 121.47°E, which is close to the Yellow Sea and Bohai Sea, with an average elevation of 0 m. Yantai-sea experiences a warm-temperature monsoonal continental climate, characterized by mild

Preprints (www.preprints.org) | NOT PEER-REVIEWED | Posted: 6 December 2023 doi:10.20944/preprints202312.0301.v1

temperatures and abundant precipitation throughout the year. The Yantai-sea is selected as an important validation site.

Table 1. Information of the seven stations selected in the study aera for validation.

No.	Station	Land cover	Study area	Longitude (°)	Latitude (°)	Elevation (m)
1	Ulansuhai	Water body	Baotou	108.7706E	40.8476N	977
2	Bare soil	Bare soil	Baotou	108.8176E	40.7978N	977
3	Kubq desert	Desert	Baotou	108.6203E	40.4551N	977
4	Baotou sand	Sand	Baotou	109.6187E	40.8659N	1296
5	Baotou Crop	Vegetation	Baotou	109.5537E	40.8708N	1295
6	Zhangye wetland	Reed wetland	HRB	100.4464E	38.9751N	1460
7	Desert	Reaumuria desert	HRB	100.9872E	42.1135N	1054
8	Yantai-sea	Water body	Yantai	121.4653E	37.5148N	0

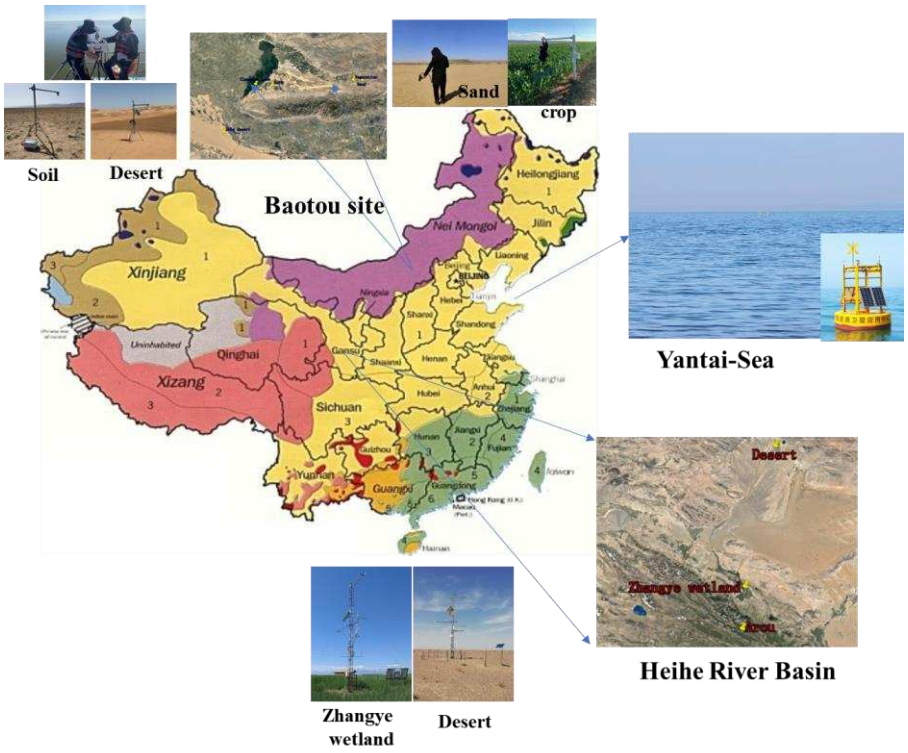

Figure 1. The study area used for validation.

2.2. ZY1-02E Data

The ZY1-02E satellite captures visible and infrared imagery to measure various parameters of the land, atmosphere, and oceans. As a cutting-edge, operational high-resolution imaging instrument, it belongs to a new generation of remote sensing technology. The ZY1-02E satellite enables the generation of various critical environmental products, such as snow and ice cover, clouds and city monitoring, sea and LST, vegetation and surface albedo, etc. Table 2 provides a comprehensive summary of its detailed spectral characteristics in its 10 spectral bands, which range from 0.45 to 12.0μm. The data is obtained from both the VNIC and IRS sensors. The VNIC sensor has 9 bands with a spatial resolution of 2.5m (Pan) and 10m (multispectral) at nadir. Additionally, the

Preprints (www.preprints.org) | NOT PEER-REVIEWED | Posted: 6 December 2023 doi:10.20944/preprints202312.0301.v1

IRS sensor includes one thermal infrared band with a 16m spatial resolution at nadir, specifically designed for LST retrieval. The ZY1-02E VNIC and IRS spectral response functions are shown in Figure 2 and 3.

Table 2. Spectral Characteristics of ZY1-02E VNIC/IRS.

Bands	Bands No.	Spectral Range(μm)	Resolution(m)	NEDT/SNR
VNIC	Pan	0.45~0.90	2.5	≥28dB@sun altitude angle is 30° and surface reflectance is 0.03 ≥48dB@sun altitude angle is 70° and surface reflectance is 0.5
	B1	0.45~0.52	10	
	B2	0.52~0.59	10	
	B3	0.63~0.69	10	
	B4	0.77~0.89	10	
	B5	0.40~0.45	10	
	B6	0.59~0.625	10	
	B7	0.705~0.745	10	
	B8	0.860~1.040	10	
IRS	B9	7~12	16	NEΔT≤0.1K@300K

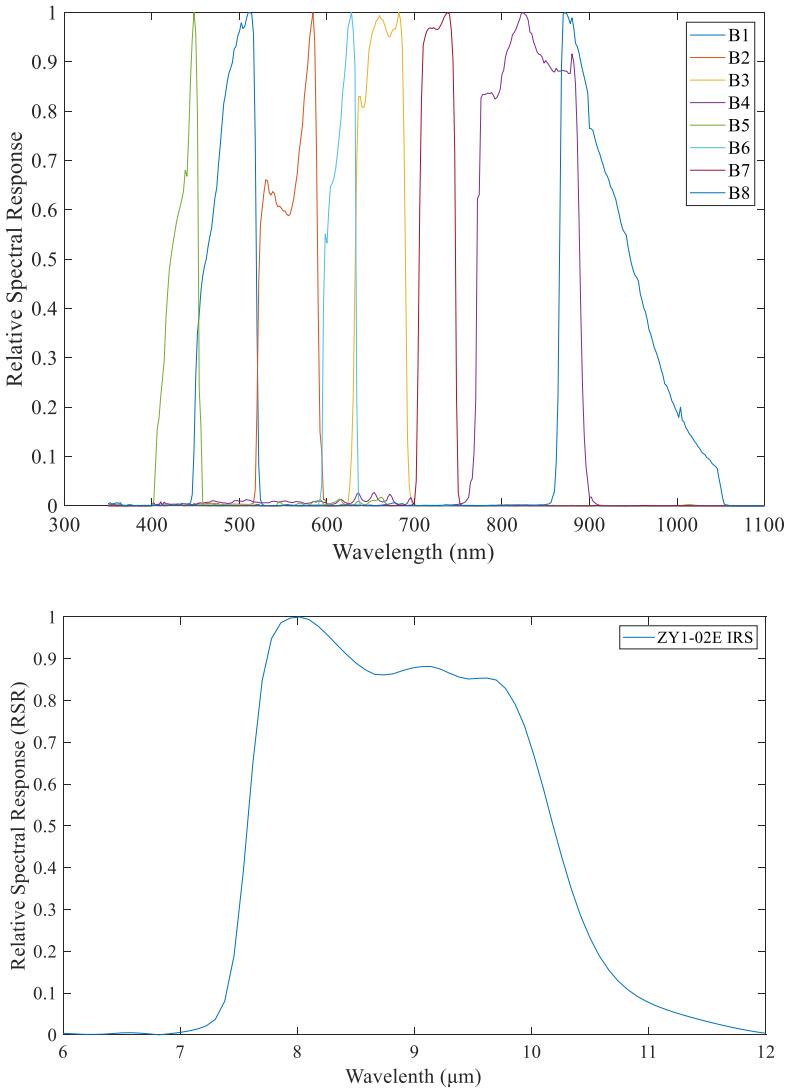

Figure 2. Relative spectral response function (a) ZY1-02E VNIC; (b) ZY1-02E IRS.

Preprints (www.preprints.org) | NOT PEER-REVIEWED | Posted: 6 December 2023 doi:10.20944/preprints202312.0301.v1

Figure 3 shows the transmittance of atmospheric water vapor and ozone from 7 μm to 12 μm using MODTRAN US 1976 Standard atmosphere. The minimum of ozone transmittance ranging from 9 to 10 μm is nearly 0.2. Meanwhile, the IRS channel covers both water vapor continues absorption and line absorption, especially 8~9 μm. Compared to traditional thermal infrared sensor used for LST estimation, the ZY1-02E IRS channel is strongly influenced by water vapor and ozone.

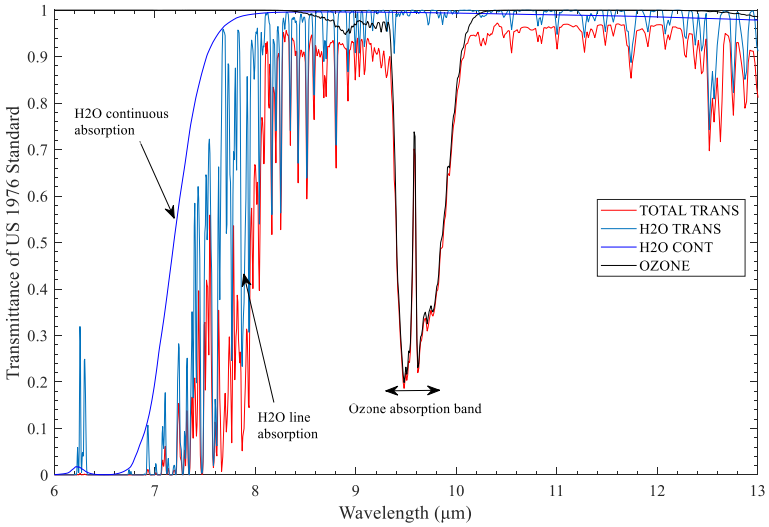

Figure 3. Total transmittance of H2O and ozone from 7 μm to 12 μm.

2.3. MODIS Data

The Moderate Resolution Imaging Spectroradiometer (MODIS), onboard the NASA Aqua and Terra Earth Observing System satellites, is one of the key instruments mainly used to observe biological and physical processes around the world. MODIS provides per-pixel LST (https://modis.gsfc.nasa.gov/data/dataprod/mod11.php) and Sea Surface (SST, https://oceancolor.gsfc.nasa.gov/cgi/browse.pl?sub=level3&prm=SST) products, covering from 5-minute temporal to multi-day average In this paper, two temperature products (i.e., MOD11_L2 and SST data) were used to validate the accuracy of the WVS-based method. The spatial resolution of both of temperature products is 1 km. MOD11_L2 LST product is retrieved by using the generalized split-window algorithm[29]. A comparison was performed between the MOD11_L2 LST and ground measurements at several sites: Brookings, Audubon, Canaan Valley, and Black Hills [30]. Results show that the absolute biases and RMSEs between MOD11_L2 LST and ground measurements were less than 0.8K and 1.7K, respectively.

2.4. The ASTER Spectral Library

The Advanced Spaceborne Thermal Emission and Reflection Radiometer (ASTER) spectral library v2.0 [31], developed jointly by the Jet Propulsion Laboratory (JPL), Johns Hopkins University (JHU), and the United States Geological Survey (USGS), comprises a comprehensive collection of data. It encompasses over 2300 spectra covering a broad range of materials, such as vegetation, man-made materials, soil, minerals, rocks, water, ice, and snow. The wavelength range covered is from 0.4 μm to 15.4 μm, with specific wavelengths falling between 3.0 μm and 14.5 μm. From this library, 108 emissivity spectra were selected to represent various surface features including 70 soil/mineral types, 28 vegetation types, and 10 man-made material types.

 doi:10.20944/preprints202312.0301.v1

2.5. ERA5 Atmospheric Profiles

In order to determine the LST, atmospheric correction is essential. In this paper, the European Centre for Medium-Range Weather Forecasts (ECMWF) ERA5 atmospheric profile dataset was used to obtain the atmospheric parameters by using the radiative transfer code (MODTRAN 5.3) developed by AFRL/VSBT in collaboration with Spectral Sciences, Inc. ERA5, the fifth-generation ECMWF reanalysis, offers global climate and weather data spanning the past 8 decades. The dataset begins from 1940, replacing the ERA-Interim reanalysis. By leveraging the ERA5 profiles, atmospheric parameters such as atmospheric transmittance, atmospheric downwelling and upwelling radiances are derived.

ERA5 profiles provide geopotential height, temperature, relative humidity information at 37 pressure levels and total column ozone on a 0.25° × 0.25° grid, with updates every hour in UTC time. ERA5 atmospheric profiles provide the pressure, geopotential height, air temperature, relative humidity, et al., which has 0.25° of the spatial resolution, 37 pressure levels (1, 2, 3, 5, 7, 10, 20, 30, 50, 70, 100, 125, 150, 175, 200, 225, 250, 300, 350, 400, 450, 500, 550, 600, 650, 700, 750, 775, 800, 825, 850, 875, 900, 925, 950, 975, 1000), 48 km height, and 1-hour temporal resolution. It is worth noting that, due to the wide spectrum of ZY1-02E covering the ozone absorption band, the total column ozone is also applied in the algorithm process and simulation for WVS coefficients. The ERA5 profiles were used to calculate the atmospheric transmittance, upwelling and downwelling radiances with the aid of MODTRAN 5.3.

2.6. In Situ Data

At Baotou site, SI-111 thermometers with a spectral range of 8~12 μm were employed to measure the temperature of various surfaces, including sand, crop, Ulansuhai Lake, bare soil and Kubq desert, etc. At Baotou site, two thermometers were distributed in sand area, bare soil, Kubq desert, and four thermometers were distributed in crop area to capture the in-situ field LSTs, and the temporal sampling interval is 2 second and an altitude of approximately 2.0 m. An additional SI-111 thermometer was used to observe the sky at an angle of 53° relative to the zenith and measure the atmospheric downwelling radiance to correct for the atmospheric effect. For Ulansuhai Lake, a 102F Fourier Transform Infrared Spectroradiometer (FTIR) with a spectrum ranging from 2 to 16 μm, a spectral resolution of 4 cm^{-1}, and a field of view (FOV) of 4.8° and two thermometers were deployed on boat to measure the water temperature. At Heihe River Basin, two SI-111 thermometers are mounted at 6m, facing due south, with the probe facing straight down to measure the LST. Land emissivity measurements were performed using the 102F FTIR.

Two automatic water observation buoys in Yantai-Sea, equipped with an automatic weather station to measure wind speed, wind direction, atmospheric temperature, humidity, pressure, rainfall. SI-111 thermometer is used to measure the sea temperature.

Next equation was used to calculate the in situ LSTs from surface-leaving radiance and atmospheric downwelling radiance:

$$T_s = B^{-1}\left(\frac{L-(1-\varepsilon)L_{atm\downarrow}}{\varepsilon}\right) \quad (1)$$

Where, T_s represents LST, B denotes the Planck function, L is radiance measured by the SI-111 radiometer, ε is the channel-effective Land Surface Emissivity (LSE) specifically for SI-111 thermometer, and $L_{atm\downarrow}$ is atmospheric downwelling radiance calculated by the spectral response function of the SI-111 thermometer.

In this study, several natural scenes (refer to Figure. 4) were selected to evaluate the accuracy of LST estimated from the ZY1-02E IRS data. Table 3 provides a summary of the main technical characteristics of the thermal instruments. Figure 4 illustrates the primary attributes of the measurement targets.

Preprints (www.preprints.org) | NOT PEER-REVIEWED | Posted: 6 December 2023 doi:10.20944/preprints202312.0301.v1

Table 3. Main technical specifications for the thermal instruments.

Instrument	Spectral Range (μm)	Operating environment (°C)	Accuracy	Resolution	FOV (º)
SI-111	8~14	-55~80	±0.2 K	0.1 K	44
KT-15	9.6~11.5	0~55	±0.5 K	0.06 K	2
102F	2~16	15~35	1 cm^{-1}	4 cm^{-1}	4.8

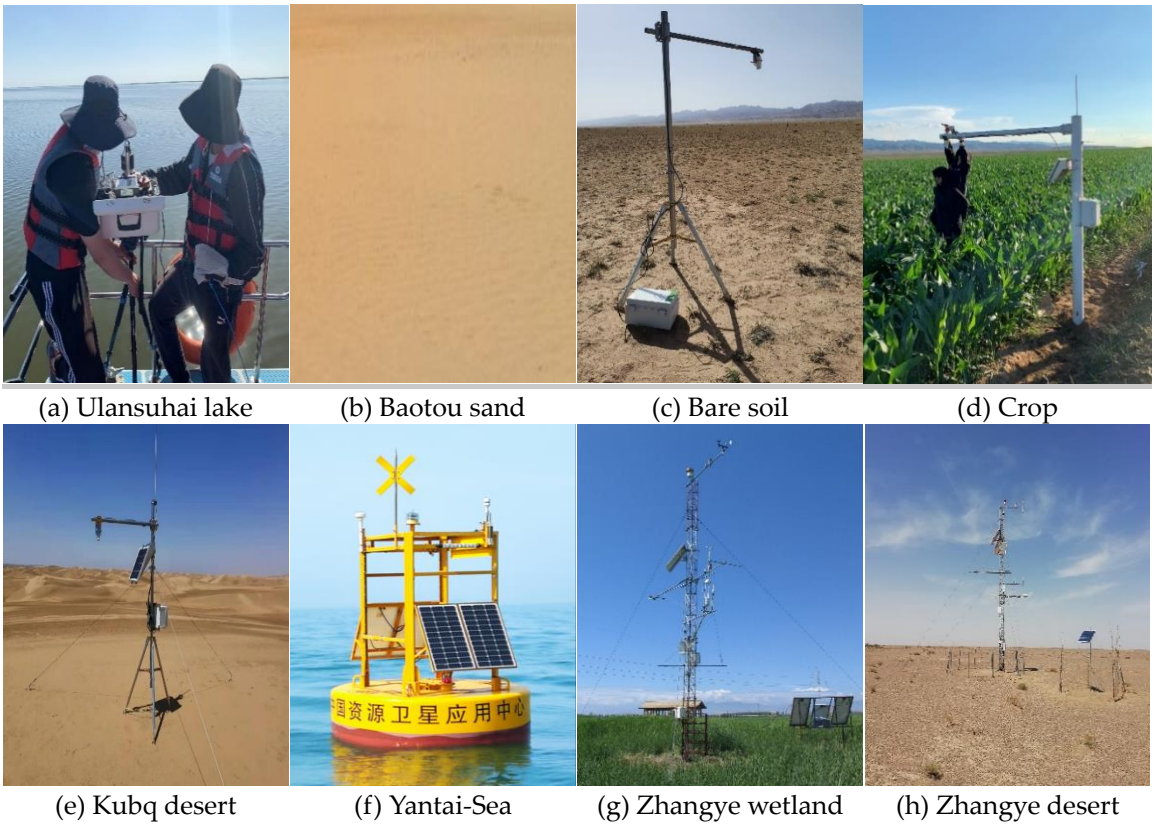

(a) Ulansuhai lake (b) Baotou sand (c) Bare soil (d) Crop

(e) Kubq desert (f) Yantai-Sea (g) Zhangye wetland (h) Zhangye desert

Figure 4. Photos of targets in study area.

3. Methodologyas

3.1. WVS-Based LST Method

The theoretical basis of radiative transfer in the TIR spectral region (8–14 m) has been developed[14]. In the case of a cloud-free atmosphere under local thermodynamic equilibrium, the radiative transfer equation (RTE) can approximately be expressed as:

$$L_\lambda(T) = \tau_\lambda \left[\varepsilon_\lambda B_\lambda(T_s) + (1 - \varepsilon_\lambda) L_{atm\_\lambda}\downarrow \right] + L_{atm\_\lambda}\uparrow \quad (2)$$

where, T is the at-sensor brightness temperature (BT), $L_\lambda(T)$ is the at-sensor radiance at wavelength λ. τ_λ is the atmospheric transmittance at wavelength λ. ε_λ is the land surface emissivity. $B_\lambda(T_s)$ is the Planck function of the wavelength λ. T_s is the LST. $L_{atm\_\lambda\uparrow}$ is the atmospheric upwelling radiance, and $L_{atm\_\lambda\downarrow}$ is the downwelling radiance. Obviously, the atmospheric parameters were estimated by using a radiative transfer code, such as MODTRAN, with atmospheric profiles and elevation data. Thus, the LST based on RTE method is derived from the at-sensor radiance.

Preprints (www.preprints.org) | NOT PEER-REVIEWED | Posted: 6 December 2023 doi:10.20944/preprints202312.0301.v1

As well-known, the existing single-channel method for LST retrieval, the reanalysis atmospheric profile dataset, such as European Centre for Medium-Range Weather Forecasts (ECMWF), National Centers for Environmental Prediction (NCEP), etc., is generally preferred to correct the atmospheric effect [32, 33]. However, the reanalysis of atmospheric profile data has certain uncertainty, which will influence the accuracy of atmospheric transmittance and atmospheric upward/downward radiance, and then the retrieval accuracy of LST will be affected. The WVS-based method proposed by Tonooka [34, 35] is based on the standard atmospheric correction algorithm for ASTER/TIR. A significant enhancement of this method involves determining a water vapor scaling factor γ, which serves to mitigate the errors resulting from multiple sources. These errors include not only a bias error in the water-vapor profile but also random errors in the water-vapor profile, errors in the air temperature profile, and elevation errors. Since all of these errors contribute to the bias error in the water-vapor profile. Once an appropriate γ is determined, the improved atmospheric parameters are calculated by:

$$\tau(\theta,\gamma)=\tau(\theta,\gamma_1)^{(\gamma^\beta-\gamma_2^\beta)/(\gamma_1^\beta-\gamma_2^\beta)}\cdot\tau(\theta,\gamma_2)^{(\gamma_1^\beta-\gamma^\beta)/(\gamma_1^\beta-\gamma_2^\beta)} \tag{3}$$

$$L_{atm\_\lambda\uparrow}(\theta,\gamma)=L_{atm\_\lambda\uparrow}(\theta,\gamma_1)\cdot\frac{1-\tau(\theta,\gamma)}{1-\tau(\theta,\gamma_1)} \tag{4}$$

$$L_{atm\_\lambda\downarrow}(\gamma)=a+bL_{atm\_\lambda\uparrow}(0,\gamma)+cL_{atm\_\lambda\uparrow}(0,\gamma)^2 \tag{5}$$

$$\gamma=\frac{U'}{U}=\frac{\omega(z)'}{\omega(z)} \tag{6}$$

where, γ is water vapor scaling factor . U and U' are the total water vapor content of atmospheric parameters for water-vapor profile P and P′, respectively, where P′ is a water-vapor profile scaled from a water-vapor profile P by a factor of γ. $\omega(z)$ and $\omega(z)'$ are water-vapor amounts at an arbitrary height Z. γ_1 and γ_2 are appropriate different values (e.g., γ_1=1 and γ_2 =0.7 in this paper).

$$\gamma=\left(\ln\left(\frac{\tau(\gamma_2)^{\gamma_1^\beta}}{\tau(\gamma_1)^{\gamma_2^\beta}}\cdot\left(\frac{B(T_g)-\dfrac{L^\uparrow(\gamma_1)}{1-\tau(\gamma_1)}}{B(T_{\text{sensor}})-\dfrac{L^\uparrow(\gamma_1)}{1-\tau(\gamma_1)}}\right)^{(\gamma_1^\beta-\gamma_2^\beta)}\right)/\ln\left(\frac{\tau(\gamma_2)}{\tau(\gamma_1)}\right)\right)^{1/\beta} \tag{7}$$

where， $B(T_g)$ is at-surface radiance, i.e., $B(T_g)=\varepsilon B(T_s)+(1-\varepsilon)L^\downarrow$.

From Figure 3, it can be found that the IRS sensor has been influenced by atmospheric water vapor and ozone. Therefore, in this paper, the WVS coefficients were simulated by using the global atmospheric profile library, i.e. the Thermodynamic Initial Guess Retrieval (TIGR) database, including band model parameter β, regression coefficient a, b and c of atmospheric downward radiation. The TIGR atmospheric profile database contain 2311 representative atmospheric situation. Each profile records the atmospheric pressure, temperature, humidity and ozone content. The atmospheric transmittance under different water vapor scaling factors γ (0.7, 0.9 and 1.0, respectively) was obtained by MODTRAN 5.3 in band model parameter, and the parameters

 doi:10.20944/preprints202312.0301.v1

β were obtained by least-square regression. β is equal to 1.4072 calculated from large amount of simulation data. The coefficients a, b and c can be obtained from the simulated the atmospheric downwelling and upwelling data, where whose are -0.3630, 2.2013 and -0.1080, respectively. Obviously, the calculation of atmospheric parameters takes into account the influence of water vapor and ozone, which provides more accurate atmospheric data for LST inversion.

3.2. Land Surface Emissivity Inversion

The estimation of land surface emissivity (LSE) relies on the fraction vegetation coverage method (FVC), which integrates two constant emissivity values representing the bare ground and full vegetation conditions of each pixel. The real-time emissivity is then adjusted according to the FVC. The classification of land surface into distinct types necessitates the adoption of varied processing approaches owing to their diverse thermal emission characteristics. The inland water and full vegetation emissivities are directly converted from the mean value determined according to ASTER spectral library dataset, and bare soil emissivity is calculated based on the relationship between emissivity and reflectance of red band (Tang et al. 2015), i.e., $\varepsilon = a + b \cdot \rho_{red}$. Where a and b are the channel-dependent regression coefficients, and ρ_{red} is the reflectance of red band. For mixed pixel, the emissivity can be expressed as a linear relationship between the bare soil and vegetation fraction [36]:

$$\varepsilon = \varepsilon_{\mathrm{v}} f_{\mathrm{v}} + \varepsilon_{\mathrm{s}} (1 - f_{\mathrm{v}}) + d\varepsilon \tag{8}$$

where ε_{v} and ε_s are the emissivity of the vegetation and bare soil, respectively, and f_{v} is the Fractional Vegetation Coverage (FVC) [37]:

$$f_{\mathrm{v}} = \frac{NDVI - NDVI_{\min}}{NDVI_{\max} - NDVI_{\min}} \tag{9}$$

where Normalized Difference Vegetation Index(NDVI) is acquired from the target pixel, where $NDVI_{\max}$ and $NDVI_{\min}$ are calculated from the full vegetation and bare soil pixels in the whole image.

$$d\varepsilon = 4(1 - \varepsilon_s)\varepsilon_v F f_v (1 - f_v)^2 \tag{10}$$

where, *F* is the shape factor depending on the vegetation structure information, in which F is set up to be 0.55[38].

In total, the emissivity can be written as Eq. (11), where pixels with NDVI values below 0 are considered as water body ($\varepsilon=\varepsilon_{water}$). The pixels with NDVI values below 0.2 are considered as bare soil. NDVI values above 0.5 represents fully vegetation pixels. Therefore, the pixels with NDVI values range from 0.2 to 0.5 are considered as mixture of soil and vegetation [39, 40].

$$\varepsilon = \begin{cases} \varepsilon_{\mathrm{water}}, & \mathrm{NDVI}<0 \\ \varepsilon = a + b \cdot \rho_{red}, & 0 \le \mathrm{NDVI} < 0.2 \\ \varepsilon_{\mathrm{v}} f_{\mathrm{v}} + \varepsilon_{\mathrm{s}} (1 - f_{\mathrm{v}}) + d\varepsilon, & 0.2 \le \mathrm{NDVI} \le 0.5 \\ \varepsilon_{\mathrm{v}}, & \mathrm{NDVI} > 0.5 \end{cases} \tag{11}$$

where, $\varepsilon_{\mathrm{water}}$ is emissivity of water, ε_s is emissivity of soil, and ε_v is emissivity of vegetation. ρ_{red} is reflectance of red band.

Preprints (www.preprints.org) | NOT PEER-REVIEWED | Posted: 6 December 2023 doi:10.20944/preprints202312.0301.v1

3.3. Atmospheric Parameters Inversion

To obtain the atmospheric parameters for each pixel of ZY1-02E IRS image, the interpolation of atmospheric profiles in time and space must be performed. Temporal linear interpolation of the atmospheric parameters in terms of the time of the ERA5 profiles (https://cds.climate.copernicus.eu/cdsapp#!/dataset/reanalysis-era5-pressure-levels?tab=form) and the ZY1-02E acquisition time. Spatial interpolation of the atmospheric parameters in terms of geographic latitude and longitude of the closest four grid points. In addition, there is a certain uncertainty in the reanalysis of atmospheric profile data, water vapor scaling factor γ should be calculated by simulation data using WVS-based LST method. Then, the modified atmospheric parameters can be obtained.

3.4. WVS-Based LST Retrieval

DN values in ZY1-02E IRS band data should be converted to top of the atmosphere (TOA) radiance using the calibration coefficients provided in the metadata file.

$$L = a \cdot DN + b \tag{12}$$

Where, L is TOA radiance, DN is digital number of IRS data, a and b are calibration coefficients.

In addition, the TOA radiance should be converted to TOA brightness temperature (BT). Considering the wide spectral range (7~12μm) of ZY1-02E IRS sensor, the look-up table between radiance and temperature of ZY1-02E should be set up from 200K to 400K with a step of 0.1K. The flow chart of LST retrieval from ZY1-02E IRS data is shown in Figure 5.

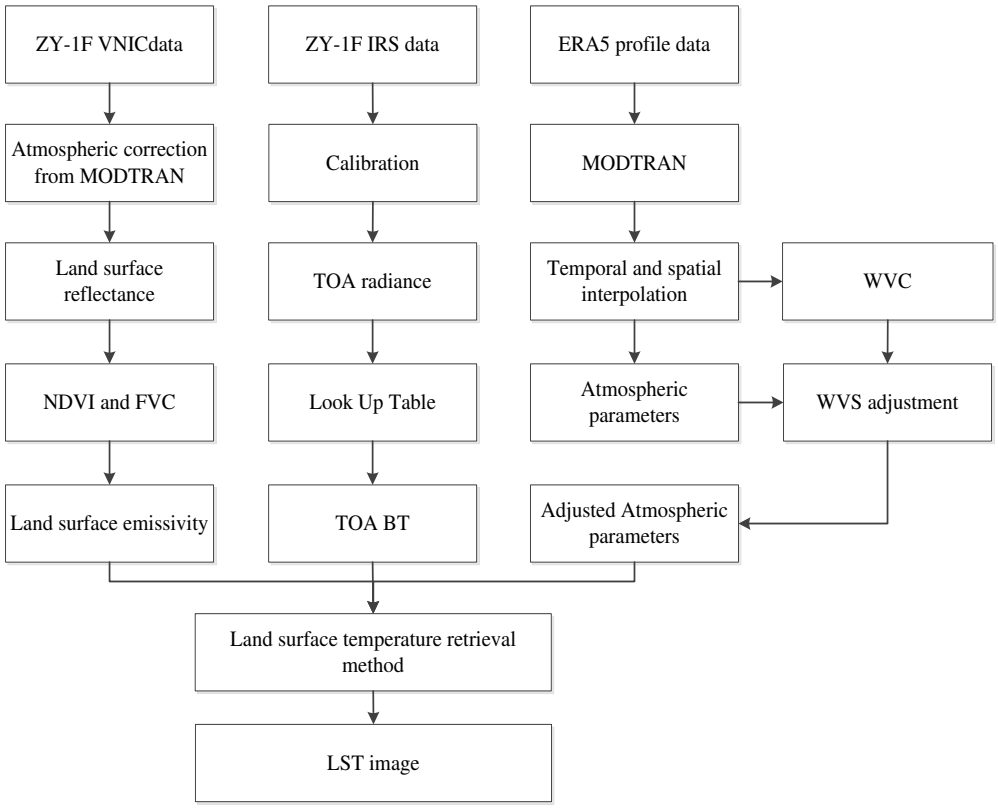

Figure 5. Flow chart of LST retrieval from ZY1-02E IRS data.

4. Results

4.1. LST Results

The LST was estimated from ZY1-02E IRS data using a WVS-based method. Based on the FVC and NDVI calculated with land surface reflectance, the emissivity for Ulansuhai, Kubq desert, Baotou

Preprints (www.preprints.org) | NOT PEER-REVIEWED | Posted: 6 December 2023 doi:10.20944/preprints202312.0301.v1

desert, Zhangye wetland, Desert and Yantai-sea sites are estimated. Emissivity measurements for bare soil were obtained on three different days (July 7th, 10th, 13th) due to variations in local FVC and NDVI.

The inversed LST images of study area A (Baotou site) derived from ZY1-02E IRS data, are presented in Figure. 6. We selected two specific days (i.e.,July 7th, 10th, 2022) of ZY1-02E IRS images that cover the Baotou site. The average UTC time of ZY1-02E overpass at the Baotou site is 03:50. Figure 6 demonstrates that the temperature of Ulansuhai lake during local noon is typically lower than other landscapes, while bare soil and sand exhibit higher temperatures. The reflectance of water bodies exceeds that of other land cover types.

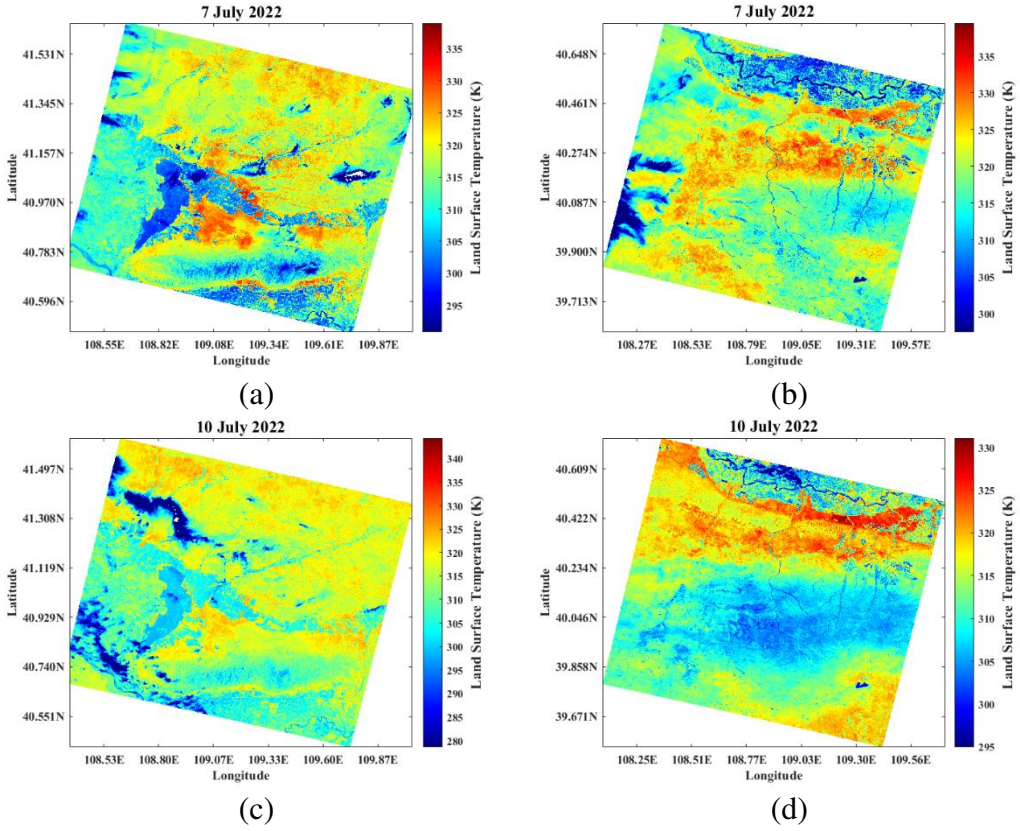

Figure 6. The retrieved LST images of study area A (Baotou site) from ZY1-02E IRS data based on WVS method; (a, c) The retrieval LST images of Ulansuhai lake, Baotou sand, crop and Bare soil. (b, d) The retrieval LST images of Kubq desert.

4.2. Validation

Two validation methods are selected, i.e., based on in-situ data and based on cross-validation with MODIS LST product, employed to evaluate the LST inversion accuracy.

4.2.1. Validation Based on In-Situ Data

The LST derived from the WVS-based method was evaluated by the comparison with ground measurements (GM) LST obtained from the Baotou, HRB and Yantai-Sea sites. The in-situ averaged LST before and after 10 minutes against ZY1-02E overpass time was selected as validation data compared with the inversed LST from these sites. Figure 7 shows scatterplots depicting the inversed LST versus the in situ LST at the eight sites. To quantitatively describe the accuracy of LST inversion, the bias and RMSE are calculated as evaluation index. The results in Figure. 7(a) reveal that the average bias and root mean square error (RMSE) between the WVS-based method and in situ LSTs are 0.63K and 1.62K, respectively. It shows a high agreement between the WVS method and field measurement data. Additionally, the results in Figure 7(b) indicate that the LSTs inversion in water

Preprints (www.preprints.org) | NOT PEER-REVIEWED | Posted: 6 December 2023 doi:10.20944/preprints202312.0301.v1

body, desert, sand, reed wetland and vegetation exhibit the closest proximity to the measured temperature data, with an average LST bias of 0.24, -0.17, -0.7, 0.27 and 0.27K, respectively. Comparatively, the average LST biases for the bare soil is 1.7K. And the RMSEs of these six land surface types (water body, bare soil, desert, sand, reed wetland and vegetation) are 1.39K, 1.77K, 0.53K, 0.99K, 0.42K and 0.42K, respectively.

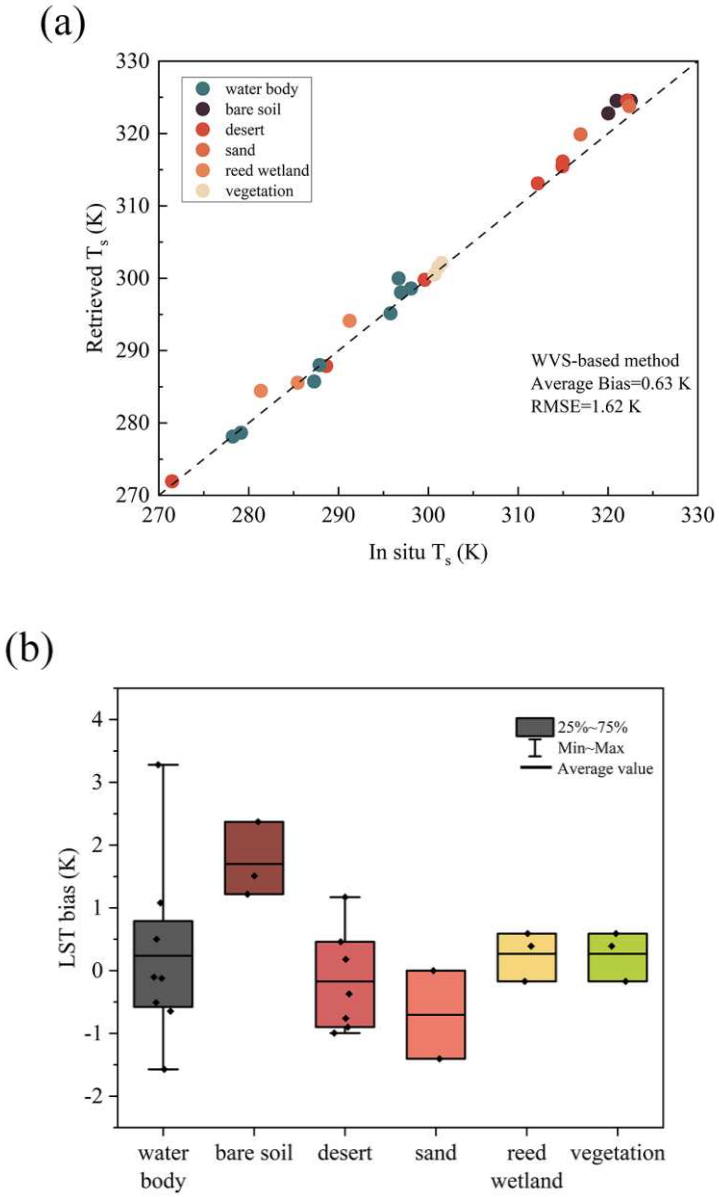

Figure 7. (a) Scatterplots of the inversed LST using WVS-based method versus the in-situ LST at six land surface types (water body, bare soil, desert, sand, reed wetland and vegetation). (b) LST bias between WVS-based method and ground measurements.

In addition, according to each surface types, the statistical analysis shows that LSTs inversion in water body, bare soil, desert, sand, reed wetland and vegetation exhibit the closest proximity to the measured temperature data, with an average LST bias and RMSE of 0.24K and 1.39K, 1.7K and 1.77K, -0.17K and 0.53K, -0.7K and 0.99K, 0.27K and 0.42K, 0.27K and 0.42K, respectively.

Preprints (www.preprints.org) | NOT PEER-REVIEWED | Posted: 6 December 2023 doi:10.20944/preprints202312.0301.v1

4.2.2. Cross-Validation Compared to MODIS LST and SST Product

As well-known, the MODIS LST product offers a high accuracy, making the MODIS Terra daily LST product (MOD11_L2) with a spatial resolution of 1km suitable for cross-validation. According to satellite overpass time, the time differences between the MOD11_L2 and ZY1-02E data range from 0 to 50 minutes for the study area A and B. To minimize the error caused by the difference due to overpass time, a temporal correction method was considered to correct the MODIS temperature product using the measured surface temperatures over the two satellites overpass time, i.e., LST = a×time + b. The coefficients a and b can be calculated by field measurement data. This is because the surface temperature shows a certain change rule over a short period of time. The ground measurement temperature data was plotted as a function of viewing time in Figure 8, and then the time-corrected MODIS LST values were obtained by a linear function expression.

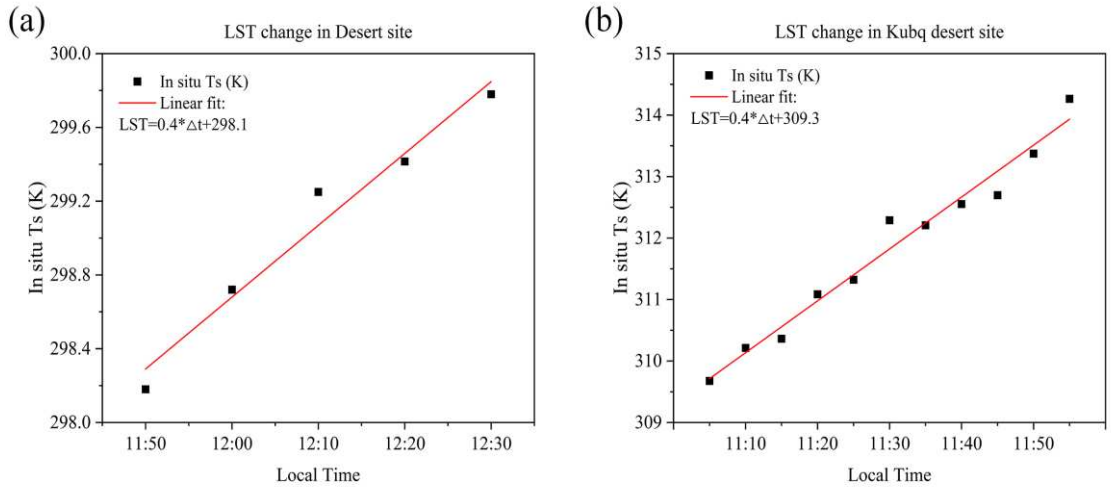

Figure 8. (a) LST change in Desert site on October 22, 2022. (b) LST change in Kubq desert site on July 7, 2022.

The results in Figure 9(a) indicates that the average bias and RMSE between the inversed LSTs from WVS-based method and MODIS LST/SST product are 0.77K and 2.0K, respectively. Figure 9(b) reveals that the LST biases between WVS-based method and MODIS LST product are consistent across five land surface types (water body, bare soil, desert, sand and reed wetland), with average biases of 0.88K, 1.5K, -0.73K, 1.3K and 3.9K, respectively. And the RMSEs are 1.75K, 1.51K, 0.71K, 1.86K and 4.05K, respectively.

Preprints (www.preprints.org) | NOT PEER-REVIEWED | Posted: 6 December 2023 doi:10.20944/preprints202312.0301.v1

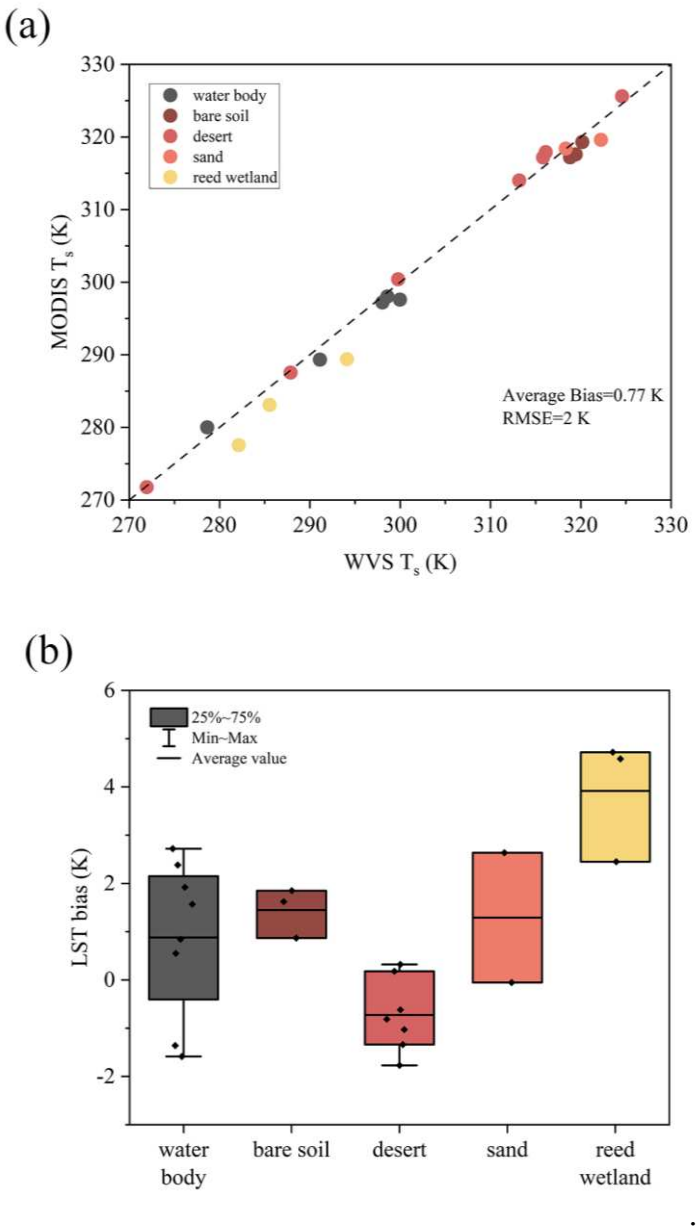

Figure 9. (a) Scatterplots of the inversed Ts (LST) versus the MODIS LST product at five land surface types (water body, bare soil, desert, sand, reed wetland). (b) LST bias between WVS-based method and MOD11_L2.

To mitigate positioning accuracy errors during the validation of the LST retrieval, we employed the average LST value of 3×3 pixels surrounding the target site in the ZY1-02E IRS images. The data collection period for the ZY1-02E IRS scenes spanned from July 2022 to March 2023. For evaluating the accuracy of LST retrieval from ZY1-02E IRS data, Figure 10 presents the results that the absolute errors (AE) between WVS-based method and ground measurement range from 0.1K to 3.5K, with an average AE of 1.31K. Moreover, the average absolute error between WVS-based method and MODIS LST&SST product is 1.82K. The dissimilarity in spatial resolution accounts for another possible reason since the ZY1-02E has a resolution of 16m, while the MODIS temperature product has a resolution of 1KM. This discrepancy can result in inaccuracies when observing bare soil, mainly due to scaling effects within the area-averaged FOV [41].

To validate the reliability of the WVS-based LST method, we conducted calculations on the variance of the LST values for the target sites and their surrounding eight pixels in the retrieval LST images, with a spatial resolution of 48m for the variance statistics. The results in Figure 10

Preprints (www.preprints.org) | NOT PEER-REVIEWED | Posted: 6 December 2023 doi:10.20944/preprints202312.0301.v1

demonstrate that the average variance of LST at the target site was 0.134K, indicating a minimal deviation in the retrieved LST for the target stations. These findings affirm that the proposed method can accurately retrieve LST from single-channel TIR data.

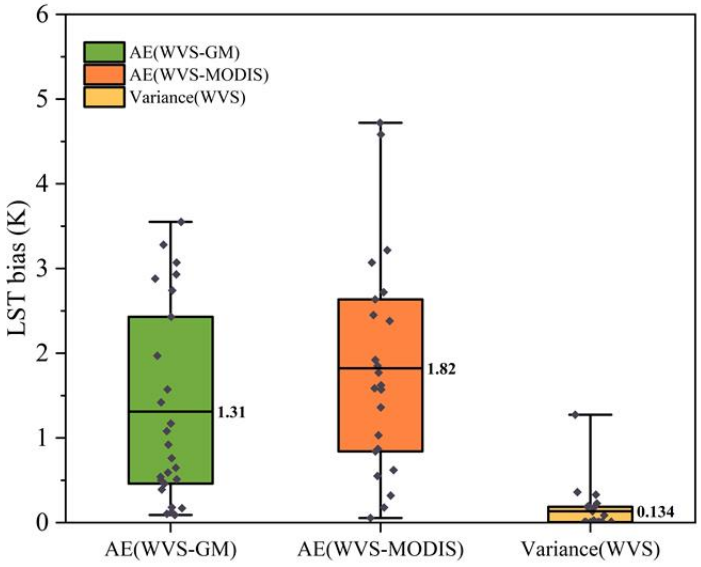

Figure 10. Evaluating accuracy of LST retrieval using WVS-based method. The boxplots are centered on the errors of retrieved LST using WVS-based method and other retrieval LST methods.

5. Discussion

In this study, the single channel algorithm based on a water vapor scaling (WVS) method proposed by Tonooka [34] to correct the error caused by uncertain atmospheric profile data was used to estimate LST from ZY1-02E thermal infrared data. In terms of the validation based on in-situ data, the WVS-based method exhibits poorer performance at bare soil and Zhangye wetland sites, as illustrated in Figure 11. The challenge of accurately defining the emissivity of Zhangye wetland and Baotou bare soil sites results in significant LST deviation, leading to reduced accuracy in LST inversion for these locations. The average LST biases between the WVS-based method and in situ LSTs for Ulansuhai, Bare soil, Kubq desert, Baotou sand, Zhangye wetland, Desert and Yantai-sea are as follows: 1.3K, 1.4K, -1.3K, 1.3K, 3.9K, -0.69K and 0.65K, respectively. Therefore, the WVS-based method demonstrates higher accuracy for the uniform land cover, such as water bodies, deserts. The results show the effectiveness of LST inversed from ZY1-02E IRS data using the WVS-based method. Although comparing to MODIS LST product, the spatial resolution of Landsat 9's Thermal Infrared Sensor 2 (TIRS-2) and ECOTRESS LST product are higher, with 100m and 70m, respectively, the transit dates for either Landsat or ECOTRESS are different with ZY1-02E. The cross-validation based on MODIS LST and SST products were performed. To ensure comprehensive coverage of the corresponding areas in the MODIS LST product, we analyzed the average LST value and LST variance using 63 pixels per site in ZY1-02E IRS images. Figure 11 illustrates that the average LST biases between the WVS-based method and MODIS are lower in Baotou sites compared to HRB sites and Yantai-sea. The vegetation area of Baotou Crop site is less than the MODIS single pixel size of 1km*1km, so the retrieval LST of the Baotou Crop was not considered in the comparison with MODIS LST product. The results of average LST bias between the WVS-based method and MODIS product for each study site indicate that the homogeneity of land cover types plays a critical role in LST retrieval across various spatial scales. This is evident that the lower LST biases can be found in water bodies, deserts, and vegetated areas compared to other mixed surface features.

This study employed two validation methods to assess the LST accuracy. The results demonstrated a close approximation between the WVS-based method and the in-situ LST, exhibiting an average bias of 0.63K. However, the study's focus was limited to six types of landscapes across

Preprints (www.preprints.org) | NOT PEER-REVIEWED | Posted: 6 December 2023 doi:10.20944/preprints202312.0301.v1

three study areas. Future research should explore a wider range of landscape types to comprehensively assess the applicability of the WVS-based LST method. Additional data samples should be collected for specific stations in future research.

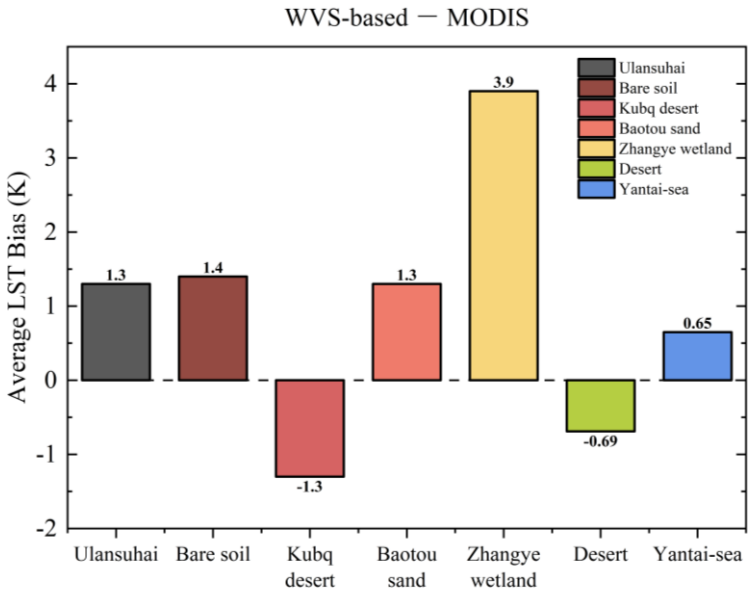

Figure 11. The LST bias retrieved by WVS-based method and MODIS in all study areas.

6. Conclusion

In this study, a water vapor scaling (WVS-based) method was used to estimate the LST from ZY1-02E IRS data and evaluate its feasibility. The ERA5 atmospheric profile dataset and the radiative transfer code were used to correct atmospheric effects. A water vapor scaling factor was used to reduce the errors in atmospheric correction caused by various atmospheric factors. Additionally, the LSE was estimated based on NDVI and FVC data. The estimated LST was validated by collecting in situ LST data from three study areas. For study area A (Baotou site), the WVS-based method showed an absolute bias of approximately 0.2 to 3.3K compared to the in situ LST, with the RMSEs ranging from 0.42 to 2.3 K. In study area B (Heihe River Basin), the LST biases ranged from 0.1 to 2.9 K, with the RMSEs between 0.5 and 2.4 K. In study area C (Yantai-sea), the SST biases ranged from 0.1 to 1.6 K, with the RMSE of ~0.8 K. In addition, according to each surface types, the statistical analysis shows that LSTs inversion in water body, bare soil, desert, sand, reed wetland and vegetation exhibit the closest proximity to the measured temperature data, with an average LST bias and RMSE of 0.24K and 1.39K, 1.7K and 1.77K, -0.17K and 0.53K, -0.7K and 0.99K, 0.27K and 0.42K, 0.27K and 0.42K, respectively. These results show that the WVS-based method can accurately retrieve LST from single-channel Thermal Infrared data though there is a wide spectrum range, i.e., 7~12μm, affected strongly by both atmospheric water vapor and ozone. However, further validation work is necessary to evaluate the method's performance across different land-cover types and geographical locations.

Acknowledge: The authors sincerely acknowledge the support of China Centre for Resources Satellite Data and Application for providing the Yantai Sea data.

Funding: This work was supported in part by the Key Program of National Natural Science Foundation of China under Grant 42130108; in part by the National Natural Science Foundation of China under Grant 42022045, International Cooperation in Science and Technology Innovation among Governments under Grant 2019YFE0127200, and Shan'xi Key Research and Development Program under Grant 2022ZDLSF06-09.

References

1. Bechtel, B., *A New Global Climatology of Annual Land Surface Temperature*[J]. Remote Sensing, 2015. **7**(3): p. 2850-2870.
2. Bright, R.M., et al., *Local temperature response to land cover and management change driven by non-radiative processes*[J]. Nature Climate Change, 2017. **7**(4): p. 296-302.https://doi.org/10.1038/nclimate3250
3. Cai, M., et al., *Investigating the relationship between local climate zone and land surface temperature using an improved WUDAPT methodology – A case study of Yangtze River Delta, China*[J]. Urban Climate, 2018. **24**: p. 485-502.https://doi.org/https://doi.org/10.1016/j.uclim.2017.05.010
4. Keenan, T.F. and W.J. Riley, *Greening of the land surface in the world's cold regions consistent with recent warming*[J]. Nature Climate Change, 2018. **8**(9): p. 825-828.https://doi.org/10.1038/s41558-018-0258-y
5. Shen, Y., et al., *Generating Comparable and Fine-Scale Time Series of Summer Land Surface Temperature for Thermal Environment Monitoring*[J]. IEEE Journal of Selected Topics in Applied Earth Observations and Remote Sensing, 2021. **14**: p. 2136-2147.https://doi.org/10.1109/JSTARS.2020.3046755
6. Myneni, R.B., et al., *Increased plant growth in the northern high latitudes from 1981 to 1991*[J]. Nature, 1997. **386**(6626): p. 698-702.https://doi.org/10.1038/386698a0
7. Peng, S.-S., et al., *Afforestation in China cools local land surface temperature*[J]. Proceedings of the National Academy of Sciences, 2014. **111**(8): p. 2915-2919.https://doi.org/doi:10.1073/pnas.1315126111
8. Tajfar, E., et al., *Estimation of surface heat fluxes via variational assimilation of land surface temperature, air temperature and specific humidity into a coupled land surface-atmospheric boundary layer model*[J]. Journal of Hydrology, 2020. **583**: p. 124577.https://doi.org/https://doi.org/10.1016/j.jhydrol.2020.124577
9. Xu, T., et al., *Evaluation of twelve evapotranspiration products from machine learning, remote sensing and land surface models over conterminous United States*[J]. Journal of Hydrology, 2019. **578**: p. 124105.https://doi.org/https://doi.org/10.1016/j.jhydrol.2019.124105
10. Li, K., et al., *A Four-Component Parameterized Directional Thermal Radiance Model for Row Canopies*[J]. IEEE Transactions on Geoscience and Remote Sensing, 2022. **60**: p. 1-15.https://doi.org/10.1109/TGRS.2021.3090451
11. Li, Z.-L., et al., *Satellite-derived land surface temperature: Current status and perspectives*[J]. Remote Sensing of Environment, 2013. **131**: p. 14-37.https://doi.org/https://doi.org/10.1016/j.rse.2012.12.008
12. Hollmann, R., et al., *The ESA Climate Change Initiative: Satellite Data Records for Essential Climate Variables*[J]. Bulletin of the American Meteorological Society, 2013. **94**(10): p. 1541-1552.https://doi.org/https://doi.org/10.1175/BAMS-D-11-00254.1
13. Li, Z.-L., et al., *Satellite Remote Sensing of Global Land Surface Temperature: Definition, Methods, Products, and Applications*[J]. Reviews of Geophysics, 2023. **61**(1): p. e2022RG000777.https://doi.org/https://doi.org/10.1029/2022RG000777
14. Li, Z., et al., *Satellite-derived land surface temperature: Current status and perspectives*[J]. Remote Sensing of Environment, 2013. **Vol.131**: p. 14-37.https://doi.org/10.1016/j.rse.2012.12.008
15. Qin, Z., A. Karnieli, and P. Berliner, *A mono-window algorithm for retrieving land surface temperature from Landsat TM data and its application to the Israel-Egypt border region*[J]. International Journal of Remote Sensing, 2001. **22**(18): p. 3719-3746.https://doi.org/10.1080/01431160010006971
16. Jiménez-Muñoz, J.C. and J.A. Sobrino, *A generalized single-channel method for retrieving land surface temperature from remote sensing data*[J]. Journal of Geophysical Research: Atmospheres, 2003. **108**(D22).https://doi.org/https://doi.org/10.1029/2003JD003480
17. Jimenez-Munoz, J.C., et al., *Revision of the Single-Channel Algorithm for Land Surface Temperature Retrieval From Landsat Thermal-Infrared Data*[J]. IEEE Transactions on Geoscience and Remote Sensing, 2009. **47**(1): p. 339-349.https://doi.org/10.1109/TGRS.2008.2007125
18. McMillin, L.M., *Estimation of Sea Surface Temperatures From Two Infrared Window Measurements With Different Absorption*[J]. Journal of Geophysical Research. Part C: Oceans, 1975. **Vol.80**(No.36): p. 5113-5117.https://doi.org/10.1029/JC080i036p05113
19. Atitar, M. and J.A. Sobrino, *A Split-Window Algorithm for Estimating LST From Meteosat 9 Data: Test and Comparison With In Situ Data and MODIS LSTs*[J]. IEEE Geoscience and Remote Sensing Letters, 2009. **6**(1): p. 122-126.https://doi.org/10.1109/LGRS.2008.2006410
20. BECKER, F., *The impact of spectral emissivity on the measurement of land surface temperature from a satellite*[J]. International Journal of Remote Sensing, 1987. **Vol.8**(No.10): p. 1509-1522.https://doi.org/10.1080/01431168708954793
21. Barton, I.J., et al., *Theoretical algorithms for satellite-derived sea surface temperatures*[J]. Journal of Geophysical Research, 1989. **Vol.94**(D3): p. 3365-3375.https://doi.org/10.1029/JD094iD03p03365

22. Caselles, V., C. Coll, and E. Valor, *Land surface emissivity and temperature determination in the whole HAPEX-Sahel area from AVHRR data*[J]. International Journal of Remote Sensing, 1997. **Vol.18**(No.5): p. 1009-1027.https://doi.org/10.1080/014311697218548
23. Gillespie, A., et al., *A temperature and emissivity separation algorithm for Advanced Spaceborne Thermal Emission and Reflection Radiometer (ASTER) images*[J]. IEEE Transactions on Geoscience and Remote Sensing, 1998. **Vol.36**(No.4): p. 1113-1126.https://doi.org/10.1109/36.700995
24. Gillespie, A.R., et al., *Residual errors in ASTER temperature and emissivity standard products AST08 and AST05*[J]. Remote Sensing of Environment, 2011. **115**(12): p. 3681-3694.https://doi.org/https://doi.org/10.1016/j.rse.2011.09.007
25. Jiménez-Muñoz, J.C., et al., *Improved land surface emissivities over agricultural areas using ASTER NDVI*[J]. Remote Sensing of Environment, 2006. **103**(4): p. 474-487.https://doi.org/https://doi.org/10.1016/j.rse.2006.04.012
26. Malakar, N.K. and G.C. Hulley, *A water vapor scaling model for improved land surface temperature and emissivity separation of MODIS thermal infrared data*[J]. Remote Sensing of Environment, 2016. **182**: p. 252-264.https://doi.org/https://doi.org/10.1016/j.rse.2016.04.023
27. Ma, C., et al., *Temperature and Emissivity Retrieval From Hyperspectral Thermal Infrared Data Using Dictionary-Based Sparse Representation for Emissivity*[J]. IEEE Transactions on Geoscience and Remote Sensing, 2023. **61**: p. 1-16.https://doi.org/10.1109/TGRS.2023.3268860
28. Liu, S., et al., *The Heihe Integrated Observatory Network: A Basin-Scale Land Surface Processes Observatory in China*[J]. Vadose zone journal VZJ, 2018. **Vol.17**(No.1): p. 1-21.https://doi.org/10.2136/vzj2018.04.0072
29. Wan, Z., *MODIS Land Surface Temperature Algorithm Theoretical Basis Documentation*[J]. 1999.
30. Wang, W., S. Liang, and T. Meyers, *Validating MODIS land surface temperature products using long-term nighttime ground measurements*[J]. Remote Sensing of Environment, 2008. **Vol.112**(No.3): p. 623-635.https://doi.org/10.1016/j.rse.2007.05.024
31. Baldridge, A.M., et al., *The ASTER spectral library version 2.0*[J]. Remote Sensing of Environment, 2009. **Vol.113**(No.4): p. 711-715.https://doi.org/10.1016/j.rse.2008.11.007
32. Yang, J., et al., *Evaluation of Seven Atmospheric Profiles from Reanalysis and Satellite-Derived Products: Implication for Single-Channel Land Surface Temperature Retrieval*[J]. Remote Sensing, 2020. **12**(5): p. 791.
33. Skoković, D., J.A. Sobrino, and J.C. Jiménez-Muñoz, *Vicarious Calibration of the Landsat 7 Thermal Infrared Band and LST Algorithm Validation of the ETM+ Instrument Using Three Global Atmospheric Profiles*[J]. IEEE Transactions on Geoscience and Remote Sensing, 2017. **55**(3): p. 1804-1811.https://doi.org/10.1109/TGRS.2016.2633810
34. Tonooka, H., *An atmospheric correction algorithm for thermal infrared multispectral data over land-a water-vapor scaling method*[J]. IEEE Transactions on Geoscience and Remote Sensing, 2001. **39**(3): p. 682-692.https://doi.org/10.1109/36.911125
35. Tonooka, H., *Accurate atmospheric correction of ASTER thermal infrared imagery using the WVS method*[J]. IEEE Transactions on Geoscience and Remote Sensing, 2005. **43**(12): p. 2778-2792.https://doi.org/10.1109/TGRS.2005.857886
36. Sobrino, J.A., J.C. Jimenez-Munoz, and L. Paolini, *Land surface temperature retrieval from LANDSAT TM 5*[J]. Remote Sensing of Environment, 2004. **Vol.90**(No.4): p. 434-440.https://doi.org/10.1016/j.rse.2004.02.003
37. Shobairi, O. and M. Li, *Dynamic Modelling of VFC from 2000 to 2010 Using NDVI and DMSP/OLS Time Series: A Study in Guangdong Province, China*[J]. Journal of Geographic Information System, 2016. **08**: p. 205-223.https://doi.org/10.4236/jgis.2016.82019
38. Zhao, E., et al., *An Operational Land Surface Temperature Retrieval Methodology for Chinese Second-Generation Huanjing Disaster Monitoring Satellite Data*[J]. IEEE Journal of Selected Topics in Applied Earth Observations and Remote Sensing, 2022. **15**: p. 1283-1292.https://doi.org/10.1109/JSTARS.2022.3143552
39. Sobrino, J.A., N. Raissouni, and Z.-L. Li, *A Comparative Study of Land Surface Emissivity Retrieval from NOAA Data*[J]. Remote Sensing of Environment, 2001. **75**(2): p. 256-266.https://doi.org/https://doi.org/10.1016/S0034-4257(00)00171-1
40. Tang, B.H., et al., *An improved NDVI-based threshold method for estimating land surface emissivity using MODIS satellite data*[J]. International Journal of Remote Sensing, 2015. **36**(19-20): p. 4864-4878.https://doi.org/10.1080/01431161.2015.1040132
41. Obata, K., T. Miura, and H. Yoshioka, *Analysis of the Scaling Effects in the Area-Averaged Fraction of Vegetation Cover Retrieved Using an NDVI-Isoline-Based Linear Mixture Model*[J]. Remote Sensing, 2012. **Vol.4**(No.7): p. 2156-2180.https://doi.org/10.3390/rs4072156

 doi:10.20944/preprints202312.0301.v1

disclaim responsibility for any injury to people or property resulting from any ideas, methods, instructions or products referred to in the content.